Application of Orthogonal Polynomial Fitting Method to Extract Gravity Wave Signals from AIRS Data Related to Typhoon Deep Convection

Zi-Liang Li[1]

[1]Ocean University of China

November 24, 2022

Abstract

Gravity waves can influence weather and climate patterns on various temporal and spatial scales in atmosphere. Despite their recognized importance, there are clearly a lack of sufficient and accurate observations from currently available satellite observing systems to satisfy the requirements of many satellite users. Common method to detect gravity waves is to measure bright temperature (BT) anomalies, which rely on an initial efficient background removal method. Before gravity waves can be extracted from Atmospheric Infrared Sounder (AIRS) raw radiances, Hoffmann and Alexander (2010) used a fourth-order polynomial fitting (4PF) method to remove the background variations. In this study, we propose a new strategy, an optimal orthogonal polynomial fitting (OPF) method using Chebyshev Polynomials as basis functions, to remove the background variations and estimate BT perturbations. By extending the classic 4PF method to the fifth-order polynomial fitting (5PF) method, and combining the Cressman interpolation (CI) method, some experiments are designed to validate the feasibility and superiority of OPF method. The results show that OPF is the optimal method to remove the limb-brightening effect in the extraction of gravity wave signals generated by typhoons. In addition, what we noticed is that an appropriate fitting orders have to be selected to get more accurate BT anomalies signals in the experiments to extract gravity wave signals.

Application of Orthogonal Polynomial Fitting Method to Extract Gravity Wave Signals from AIRS Data Related to Typhoon Deep Convection

Zi-Liang LI[1*],Ya-Ping NIU[1,2]

[1]College of Oceanic and Atmospheric Sciences, Physical Oceanography Laboratory, Ocean University of China, Qingdao, 266100, China
[1,2]Shanxi Meteorological Observatory, Xi'an, 710014, China

Key Points:

- The OPF method is proposed to extract gravity wave signals generated by typhoon deep convection systems.
- The OPF is an optimal method to remove the background BT and extract gravity signals from AIRS data.
- Although the 5PF method is inferior to the OPF method, the 5PF method is superior to the 4PF method and the CI method.

*Current address, Qingdao

Corresponding author: Zi-Liang LI, liziliang@ouc.edu.cn

Abstract

Gravity waves can influence weather and climate patterns on various temporal and spatial scales in atmosphere. Despite their recognized importance, there are clearly a lack of sufficient and accurate observations from currently available satellite observing systems to satisfy the requirements of many satellite users. Common method to detect gravity waves is to measure bright temperature (BT) anomalies, which rely on an initial efficient background removal method. Before gravity waves can be extracted from Atmospheric Infrared Sounder (AIRS) raw radiances, Hoffmann and Alexander (2010) used a fourth-order polynomial fitting (4PF) method to remove the background variations. In this study, we propose a new strategy, an optimal orthogonal polynomial fitting (OPF) method using Chebyshev Polynomials as basis functions, to remove the background variations and estimate BT perturbations. By extending the classic 4PF method to the fifth-order polynomial fitting (5PF) method, and combining the Cressman interpolation (CI) method, some experiments are designed to validate the feasibility and superiority of OPF method. The results show that OPF is the optimal method to remove the limb-brightening effect in the extraction of gravity wave signals generated by typhoons. In addition, what we noticed is that an appropriate fitting orders have to be selected to get more accurate BT anomalies signals in the experiments to extract gravity wave signals.

1 Introduction

Atmospheric gravity waves play a critical role in general circulation at scales ranging from regional weather pattern to global climate (Miller et. al., 2015). Satellite instruments are widely used to detect gravity waves, because it is not affected by weather and can observe its global structure (Moffat-Griffin, 2019;Vargas et. al., 2021). Generally, gravity wave signals are obtained by filtering out fluctuations of other scales through satellite observation data, we observed its shape and performed spectral analysis to obtain its wavelength and period (Florian and Vincent, 2001; Alexander and Barnet, 2007; Wang et. al., 2019). The AIRS detector carried on the Aqua satellite overcomes the shortcomings of insufficient resolution of previous data, and Its 4.3μm and 15μm bands are often used to discern gravity wave signals (Alexander and Barnet, 2007; Hoffmann and Alexander, 2009, 2010). Studies have shown that stratospheric temperature anomalies are directly related to BT from AIRS 4.3μm absorption band (Hoffmann and Alexander, 2009, 2010). AIRS radiation can be used to detect gravity waves with a vertical height in the range of 20km-65km and a horizontal wavelength exceeding 40 km (Alexander and Barnet, 2007).

Historically, various background removal methods have been adopted for different observation data (Alexander et. al., 2010). As early as the end of the 20th century, using sounding data detected by satellite LIMS (Limb Infrared Monitor), scientists introduced linear quadratic estimation to separate small-scale temperature perturbations from global temperature data to extract synoptic-scale stratospheric gravity wave signals (Fetzer and Gille, 1994; Eckermann and Preusse, 1999). When extracting tropospheric gravity waves from 6.7μm water vapor channel of MODIS (Moderate Resolution Imaging Spectroradiometer) detector, a filtering algorithm was used to minimize the detector-to-detector artifacts (Uhlenbrock et. al., 2007; Lyapustin et. al., 2014). Radiation perturbations separated by subtracting a third-order fitting polynomial from AMSU (Advanced Microwave Sounding Unit-A) Channels 9-14 (upper troposphere to middle stratosphere) data can extract 80hPa-2.5hPa gravity wave activity (Wu and Zhang, 2004; Eckermann et. al., 2006).

Satellite remote sensing data have improved our ability to observe gravity waves from space (Perrett et. al., 2021). However, there is still a gap between the observed temperature perturbation signals and simulated gravity waves signals. Some interpolation methods, such as CI and 4PF methods, are widely used to remove background variations in oceanic and atmospheric subjects. AIRS 4.3μm BT show a scan angle-dependent limb-brightening effect and a variable background variations due to planetary waves. Before gravity waves can be detected, Hoffmann and Alexander (2010) proposed to subtract a 4PF to remove the limb-brightening and other background effect. The subtracted 4PF is essentially the plane-parallel wave components oriented in the along-track direction. Because the angle-dependent perturbations along the track direction is not taken into account, the separated BT perturbation still contains some background variations, and it is necessary to propose a more accurate gravity wave signals extraction method.

The primary motivation for our work is to introduced a new method to retrieve gravity wave signals, also known as OPF method, which is one of the methods combining accuracy with efficiency to remove background BT. This paper is organized as follows, Section 2 is a description of the data and methods. The third part of this article is an introduction to the typhoon event. Numerical simulation of gravity waves induced by convection are set up in section 4. In Section 5, OPF method is introduced to fit AIRS background BT and extract gravity wave signals, and practical comparison are also carried out in this section. Section 6 presents the conclusions and discussions.

2 Data and Methods

2.1 Data Selection

Gravity waves are detected by AIRS on Aqua satellite via the temperature perturbation anomalies in atmosphere. AIRS instruments can provide infrared radiance spectra in 3.74-4.61μm, 6.2-8.2μm and 8.8-15.4μm wavebands. Among them, the 4.3μm and 15μm CO2 spectral bands have been extensively used to study gravity waves in the stratosphere (Alexander and Barnet, 2007; Hoffmann et. al. 2018). Here we select the AIRS 4.3μm and 15μm channel Level 1B raw radiance data to examine gravity waves signals observed in typhoon (Soulik 1307).

2.2 A local analysis method

Analysis of satellite highly accurate temperature perturbations involves removing background variations and limb-brightening effect. As is traditionally done with AIRS, The 4PF method was used to remove the background and limb-brightening effect (Hoffmann and Alexander, 2009; Holt and Alexander, 2017; Alexander and Barnet, 2007; Hoffmann et. al., 2014; Hindley et al., 2016; Wright et. al., 2017). In the present manuscript, a new OPF method, based on Chebyshev basis functions, can be also determined to remove the background and limb-brightening effect, in the cross-track as well as along track direction from AIRS raw radiances, and produce highly accurate temperature perturbations (Junkins et. al., 2013; Li et. al., 2019).

3 Typhoon Soulik (TS1307) Overview

TS1307 initially started as a tropical depression moving west across the western Pacific Ocean on July 8, and then intensified into a tropical storm at 02:00UTC on 9 July 2013. Figure 1 shows the trajectory, the minimum pressure and maximum sustained surface wind speed of storm life span. The storm rapidly strengthened in the next 24 hours, becoming a typhoon with category 1 at 08:00UTC on 9 July 2013 and a super typhoon with category 4 at 02:00UTC on 10 July 2013, and then reached its peak wind speed of $\sim 63.88 ms^{-1}$, when it moved westward along the southern periphery of subtropical high pressure system. On the afternoon of 11 July 2013, it weakened to a category 1 typhoon, and then made landfall at Taiwan island with a wind speed of $45ms^{-1}$ at 03:00UTC on 13 July 2013. TS1307 reached Fujian Province at 16:00UTC on 13 July 2013 with a wind speed of $33ms^{-1}$, and continued to move inland with heavy rain and rapidly diminishing wind speeds. TS1307 encountered a preexisting cold eddy and midlevel dry air entrained from its northwest, which coincided with its weakening before landfall. Strikingly, two concentric eye-wall (CE) structures are identified, one maintained from 07:29 UTC on July 9 to 08:32 UTC on July 10, and the other could be clearly seen from 06:30 UTC on July 11 to 16:49 UTC on July 12, which may be related to gravity waves generated by typhoon deep convection.

Our next step is to analyze whether the gravity waves are generated by deep convection in the typhoon. For the typhoon events we studied, we identified deep convection mainly by the 1231 cm^{-1} AIRS radiance channel, and a threshold of 220K was selected to detect deep convection (Hoffmann and Alexander, 2010). The AIRS cloud top BT at 8.1 μm are presented in Figure 2, where high cold clouds are identified by low BT (¡=220K), indicating the existence of deep convection. What's striking is that, deep convection is at its strongest period, when TS1307 intensifies rapidly and has peak intensity (16:42 on July 9). However, it can be clearly seen that deep convection weakens before (17:12 on July 12) and after (17:54 on July 13) TS1307 makes landfall.

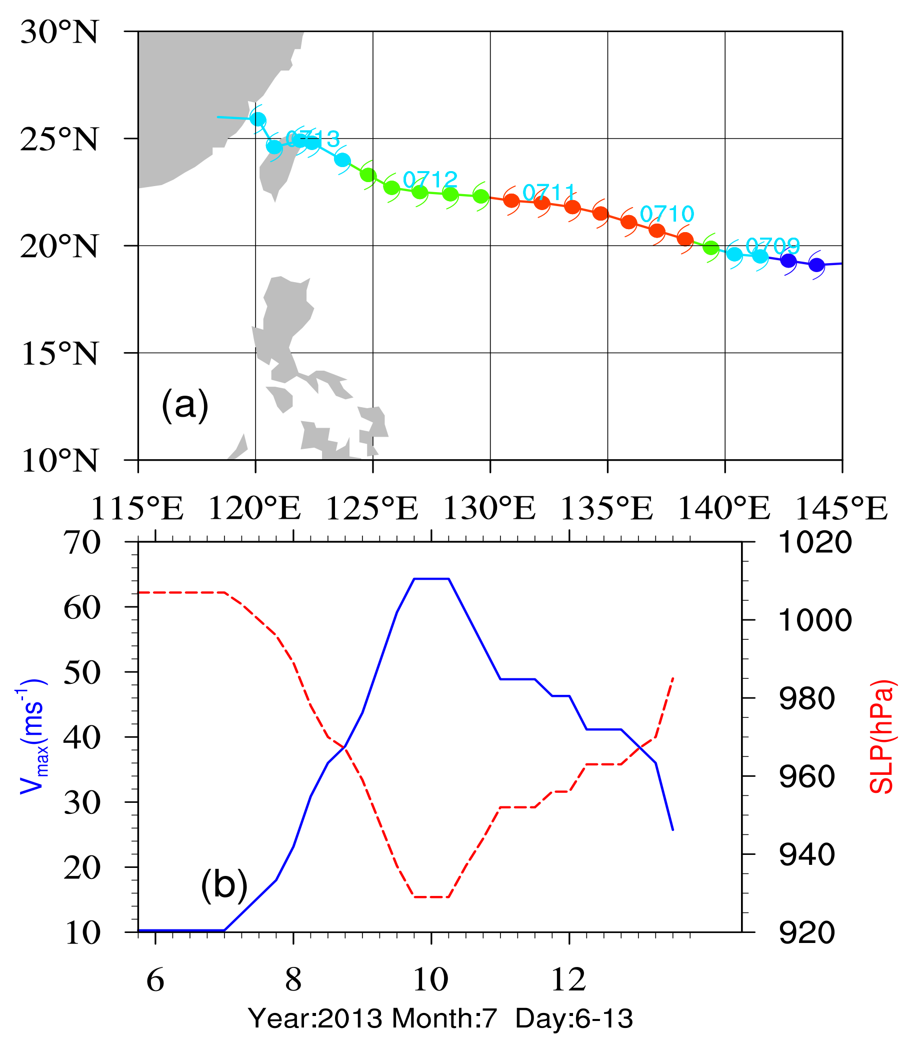

Figure 1. (a) Trajectory of storm from 6 to 13 July 2013, based on Joint Typhoon Warning Center best track data, and (b) Maximum surface wind speed and minimum central pressure of storm life span.

4 Numerical Simulation

The numerical simulation of gravity wave was performed using the Advanced Research WRF modeling system. The model was set up with a horizontal 102×86 grid points and 30km grid spacing centered on Taiwan Island (23.8^0N, 120.9^0E), a nested domain with 10 km grid spacing and a vertical sigma levels from the surface to 10 hPa, and the topmost 10 km was used as a damping layer. The simulation was integrated for 36h from 00:00 UTC 12 July to 12:00 UTC 13 July. Boundary and initial conditions were established using the National Centers for Environmental Prediction (NCEP) Final Analysis data, which had $1^0 \times 1^0$ grid resolution. The model physics schemes applied are the K-F scheme for cumulus parameterization, Lin microphysics scheme, Yon-sei University planetary boundary layer scheme, and Rapid Radiative Transfer Model for long wave radiation physics scheme (Hong et al., 2004; Hong et al., 2006; Wu et. al., 2015).

The simulated typhoon track agrees well with the observed, although it moves slightly slower than the observation. Fortunately, the simulated typhoon intensity represented by the minimum sea level pressure approaches the observed values after landfall. The magnitudes of gravity waves correlate with typhoon intensity more or less when a typhoon is in a decaying stage. To compare gravity wave characteristics in the WRF simulations and AIRS observations quantitatively, Figure 3 shows a plot of the simulated vertical velocity and potential temperature, the corresponding wavelet coefficient, local wavelet power spectrum (WPS), and its global WPS. Some wave-like cloud structures can be seen in Figure 3a and Figure 3b, indicating gravity waves moving eastward relative to typhoon. In the WRF simulation, most obvious was the significantly wavelet power through the

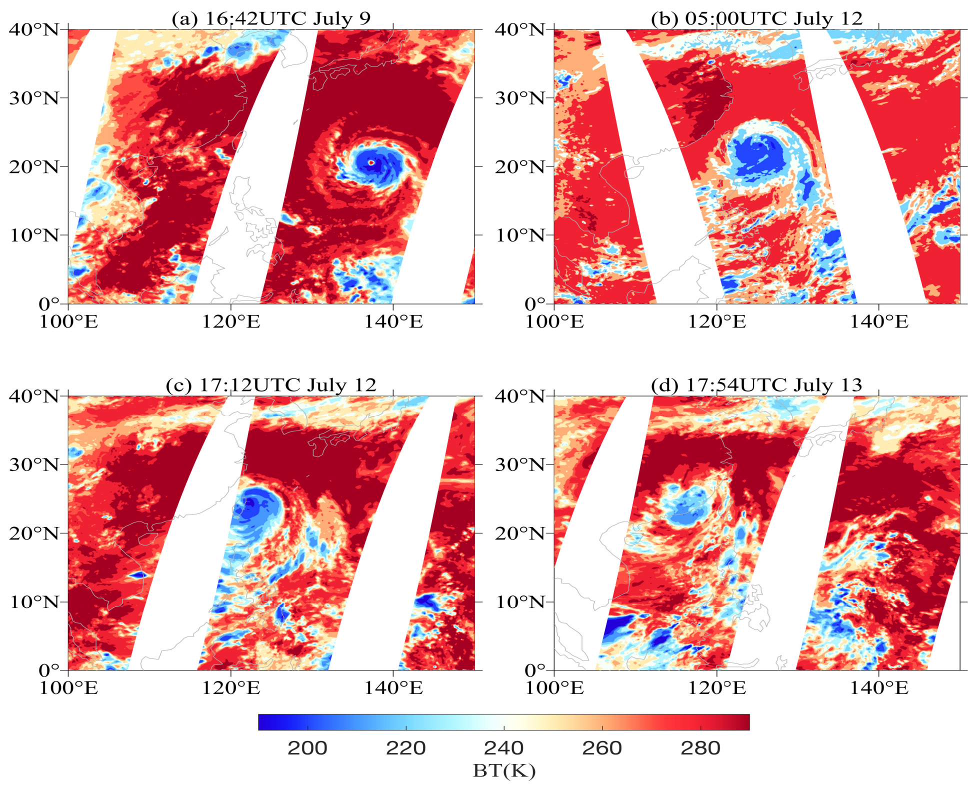

Figure 2. AIRS cloud top temperature at 8.1μm (unit: K). (a) 15:00-20:00UTC 9 July, (b) 02:00-07:00UTC 12 July, (c) 15:00-20:00UTC 12 July, (d) 15:00-20:00UTC 13 July 2013.

256 km wavelength (figure 3c). This is also illustrated by the predominant black contour band located at the 256 km wavelength on the local WPS (Figure 3d). The 256 km wavelength can be intuitively illustrated by the major peak in the global WPS (Figure 3e).

5 AIRS Observation

Analysis of AIRS radiances first require to subtract a background signals, the remaining residuals are then treated as gravity waves. In this study, a new OPF method has been developed to remove the limb-brightening effect and orthogonally fit the background signals. As is traditionally done with AIRS, the 4PF method will be also applied to extract gravity wave signals. Besides, both the 5PF and CI method are employed to evaluate and demonstrate the effectiveness of the OPF method. For the OPF method, the polynomial orders should be selected according to observation. In this study, the polynomial orders of cross-track and along-track direction are set to 6 and 7, respectively. Alternatively, for the CI method, the influence radius of CI method is initially selected as 3^0 to generate background signals. If there are at least 100 observation points within the influence radius, the background signals of that grid will be computed. Otherwise, the influence radius is increased by 0.1^0 until there are 100 observation points that fall within the radius.

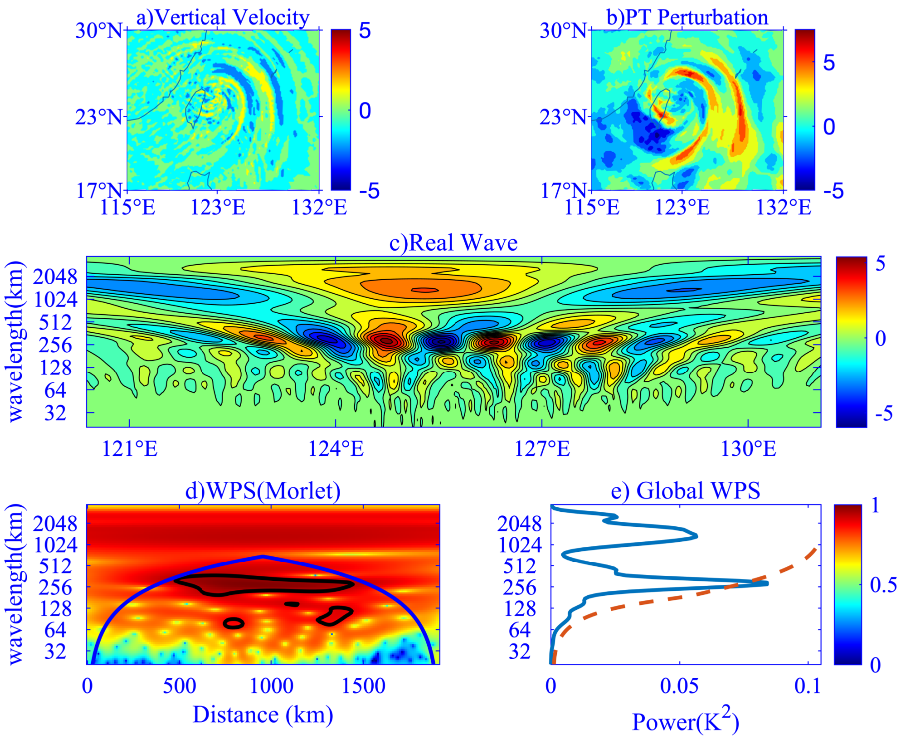

Figure 3. Wavelet spectra analysis of Simulated vertical velocity at z=26 km at 17:00 UTC, 12 July, 2013 (a) Vertical Velocity, (b) Potential Temperature, (c) Wavelet Coefficient, (d)Local WPS, (e)Global WPS.

5.1 AIRS Gravity Waves Signals

The deep convection in typhoon generates gravity waves, analysis of which can be conducted using AIRS data. Figure 4 shows the AIRS 4.3μm BT perturbations induced by TS1307 as sampled at 17:12 UTC 12 July 2013. Ring-like features indicating concentric gravity waves are easily discerned in each panel. However, gravity waves estimated by PF (4PF and 5PF) and CI methods show an intuitive spurious signals on the right-side of the scan. It has to be noted that, wave signals obtained by CI method indicate particularly obvious biases compared to all other methods on the left side of the scan. We are aware that no significant false signals with the OPF method are seen on the left and right side of the scan. These suggest that the estimated signals will apparently be more accurate if the OPF method is adopted.

AIRS BT perturbation variances by the four methods are displayed in Figure 5. If the variance exceeds the threshold of $0.05K^2$ in the range of $r < 100km$, it is assumed to be a gravity wave event. Perturbation variances by the four background removal methods determine that waves occurred behind the center of moving typhoon.

5.2 Comparison of AIRS BT Signals

The estimated background BT using the four methods are shown in Figure 6, and the black solid line indicates that the estimated background BT equal to raw radiances. From this Figure we can see that the background BT estimated by the PF and CI methods are asymmetric at the right end of the black solid line. However, the background BT estimated using the OPF method are approximately symmetric at the right end of the

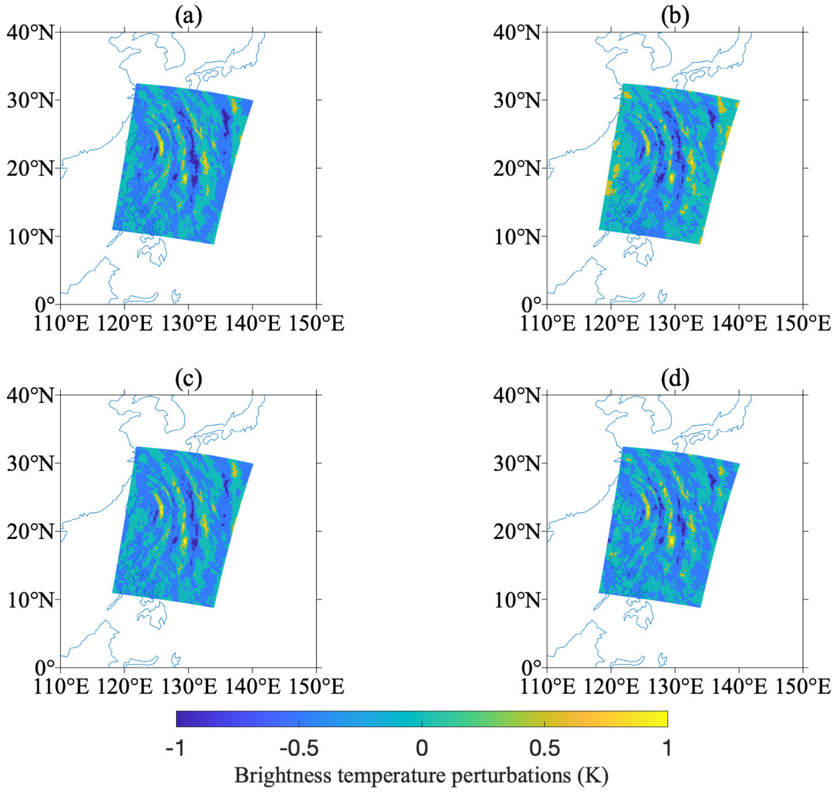

Figure 4. Gravity wave signals from AIRS radiance by four methods (a) 4PF, (b) CI, (c) 5PF and (d) OPF method in the altitude range z=30-40 km at 17:12 UTC on 12 July 2013.

black solid line. The background signal obtained by the OPF method match well with the raw radiance, which are basically adjacent to the solid line.

To further compare the pros and cons of the four methods for removing limb effects along the viewing angle, the optimum BT profile, spanning from 119.9^0E to 137.5^0E along latitude 21^0N in the altitude range 30-40km, can be expected to distinguish these four methods. The removal of the BT background signals is directly related to the characterization of the perturbation signals. The results in Figure 7 show that there are obvious differences between the four methods at both ends of the profile line. For the regions where the BT at the end of the scan is the largest, although the 5PF method is an improvement over the 4PF, there is still no obvious improvement effect. In contrast, the OPF method has the best fitted BT at the left and right end of the scan.

One way to assess how well a background BT fits a raw BT is to calculate the root mean square error (RMSE), which is a metric that tells us the average distance between the fitted BT from the four methods and the raw BT in the dataset.

The formula to find RMSE is as follows:

$$RMSE = \sqrt{\frac{SSE}{n}}, SSE = \sum_{i=1}^{n}(y_i - \widehat{y}_i)^2 \tag{1}$$

where N is the number of samples, y_i is the fitted background BT and $\widehat{y}_i$ is the raw BT.

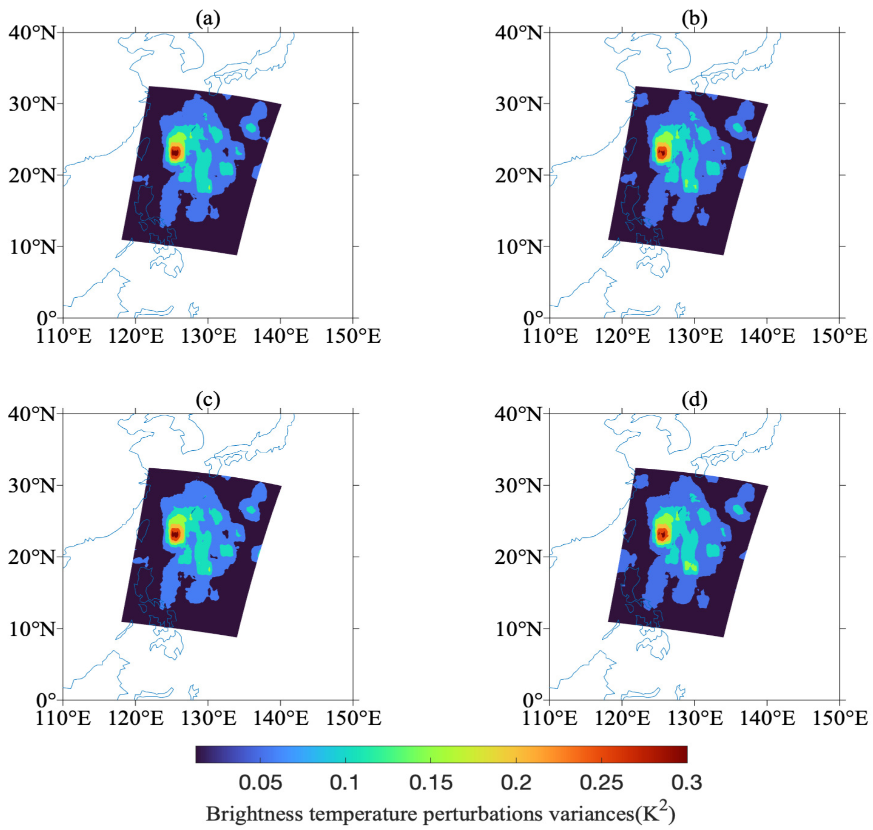

Figure 5. AIRS BT perturbation variances obtained by the four methods (a) 4PF, (b) CI, (c) 5PF and (d) OPF method.

Another way is to calculate R-Squared (RS), which indicates the correctness of the background BT and shows how well the background BT fits the raw data.

$$RS = 1 - \frac{SSE}{SST}, SST = \sum_{i=1}^{n}(y_i - \bar{y_i})^2 \tag{2}$$

where SST is the total sum of squares and $\bar{y_i}$ is the mean fitted background BT.

Here, the RMSE and RS are particularly useful for comparing the fit of these four methods. By employing both RS and RMSE as indicators, the accuracy of the fitted BT can be validated comprehensively. Figure 8 shows RMSE (blue line) and the determination coefficient RS (red line) between the background and raw BT at both ends of the profile line. As you can see from the figure 8, OPF has the lowest RMSE, which indicates that it's able to fit the background BT the best out of the four potential methods. In addition, it can be seen from Figure 8 that the RS of 5PF is the largest, and the RS of OPF is slightly weaker than that of 5PF. However, in combination with Figure 7, the 5PF mistakenly treats some real signals as gravity wave signals, which results in the fitted background BT being closer to the raw BT. Therefore, on the whole, among the four methods, the OPF method is the best for fitting the background BT at both ends of the profile line. This suggests that if we utilize the OPF method, the fitted BT will apparently be more accurate.

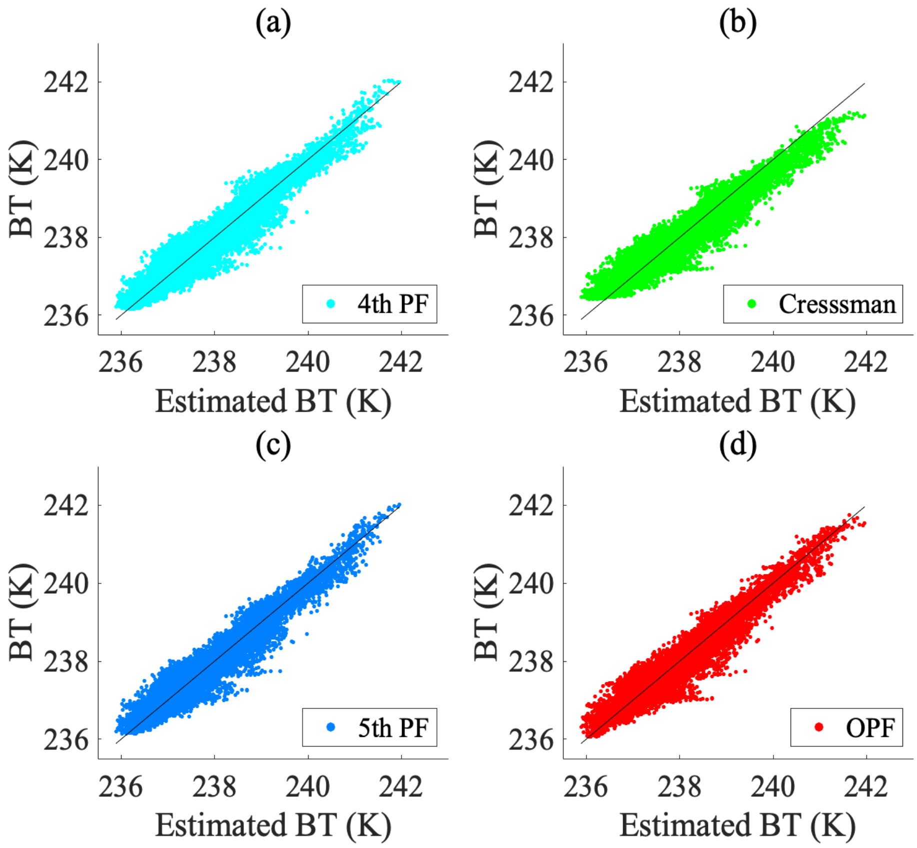

Figure 6. Comparison of Estimated BT background signals from the four methods (a) 4PF, (b) CI, (c) 5PF and (d) OPF method.

5.3 AIRS BT Wavelet Analysis

The wavelet analysis, commonly used in meteorology, is employed to represent the wave signals revealed by the BT curves in Figure 7. Local wavelet power spectrum (WPS) and global WPS of the estimated BT obtained by utilizing the four fitting methods are shown in Figure 9 and 10. The cone of influence (COI), which can isolate the background and false signals from the realistic wave signals, enclosed by the blue curve and the x-axis, represents where edge effects become important. The circles surrounded by the black curve in the figure are where the 95% confidence test was passed. The wavelength can be recognized by looking at the high-intensity spectrogram and visualizing its magnitude. It can be seen that wave signals exhibit an obvious high wavelet power through the 256 km wavelength in Figure 9 and 10. This is illustrated by the predominant black circles located at the 256km wavelength on the local WPS. The 256km wavelength also illustrated by the major peak in the global WPS and the corresponding wavelet coefficient. However, the spectrum of BT obtained by the 4PF method shows a wavelength between 256 km and 512 km, and the wavelet power by CI method also revealed two spectral peaks with wavelengths greater than 256 km. Strikingly, they are both outside the COI and beyond the 95% confidence level. These demonstrate that the BT signals obtained by the CI and 4PF method still contain strong background signals that has not been removed. It is worth noting that in the wavelet spectrum revealed by the 5PF and OPF methods, the most notable spectral peak is at 256 km wavelength, and there are

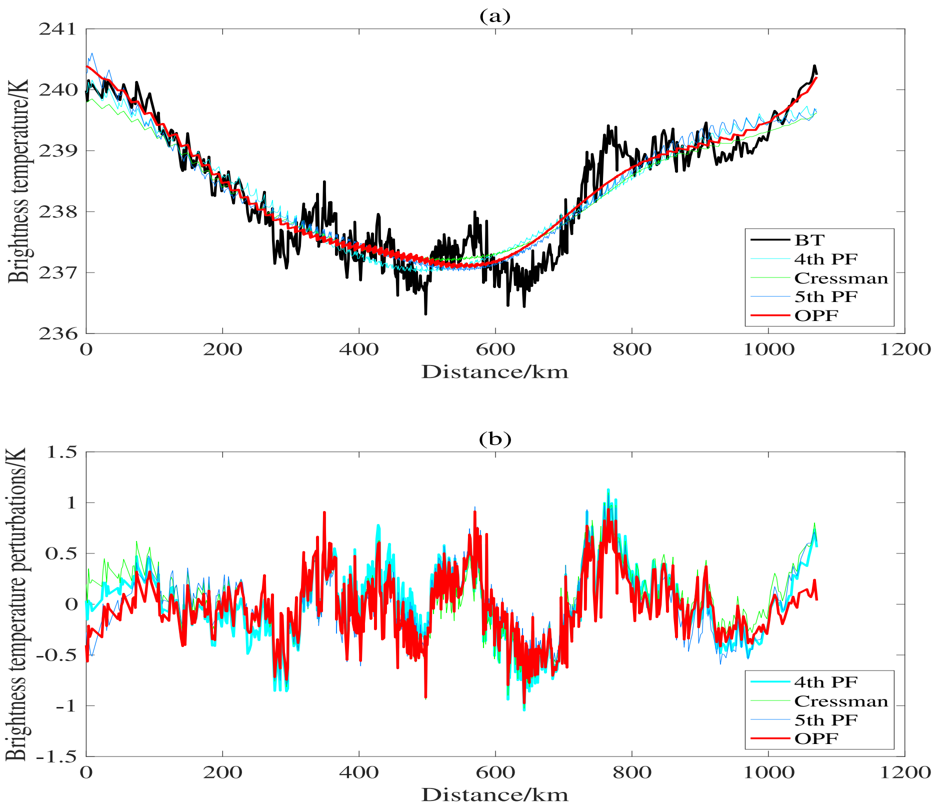

Figure 7. Comparison of BT by the four methods (a) Raw BT profile and background BT profile (b) Perturbation BT profile.

no other significant wavelengths. As can be seen from Figure 3 and 11, the gravity waves identified from the WRF simulation are reproduced well in the AIRS BT perturbations estimated by 5PF and OPF method, both in terms of horizontal wavelength and wave morphology.

To further select the optimal AIRS BT perturbation signals, the first step is to intercept 200 km at the left and right ends of the curves in Figure 7. Figure 11 shows the local and global WPS of the BT perturbations at the right end of the curves. The most striking is that the BT perturbation spectrum revealed by the 4PF method contains a significant spurious background signal. The most intuitive is that there are some significant small wave signals with wavelengths ranging from 4 to 8 km in the BT perturbation spectrum obtained by the OPF method. Relatively speaking, these indicate that BT perturbation obtained by the OPF method contains less background signals and more real signals.

6 Conclusion and Discussion

In this paper, the OPF method is presented to extract gravity wave signals from the AIRS data, and a Typhoon event is selected as an example. When applying the OPF method, we need to pay attention to the selection of the appropriate orders in x and y directions, after the polynomial coefficients are calculated based on observational data. Gravity wave signals from typhoon are successfully extracted by the OPF method with accuracy higher than CI and PF (4PF and 5PF) method. Therefore, it is validated that the OPF method can extract gravity wave signals accurately. The RMSEs of the OPF method are the smallest among those methods extracting gravity wave signals. The real waves signals by WRF simulation are reproduced well in the AIRS BT perturbation obtained by OPF method. Although the 5PF method is inferior to the OPF method, the 5PF method is superior to the 4PF method and the CI method. However, it has to be pointed out that to obtain accurate gravity wave signals, better mathematical methods

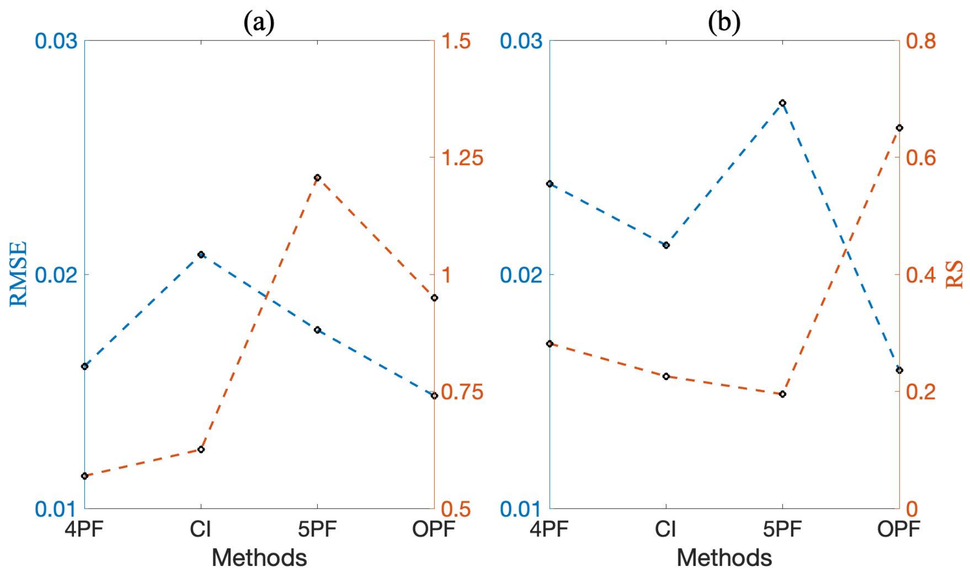

Figure 8. Comparison of RMSE and RS between the raw and the background BT fitted by the four methods (4PF, CI, 5PF and OPF method) at the (a) left and (b) right end of the profile line.

need to be proposed later to eliminate the interference caused by the satellite scanning angle and other scale signals.

Acknowledgments

This research was funded by National Natural Science Foundation of China (No. 40775069). The authors are very grateful to the editor and anonymous reviewers for their help.

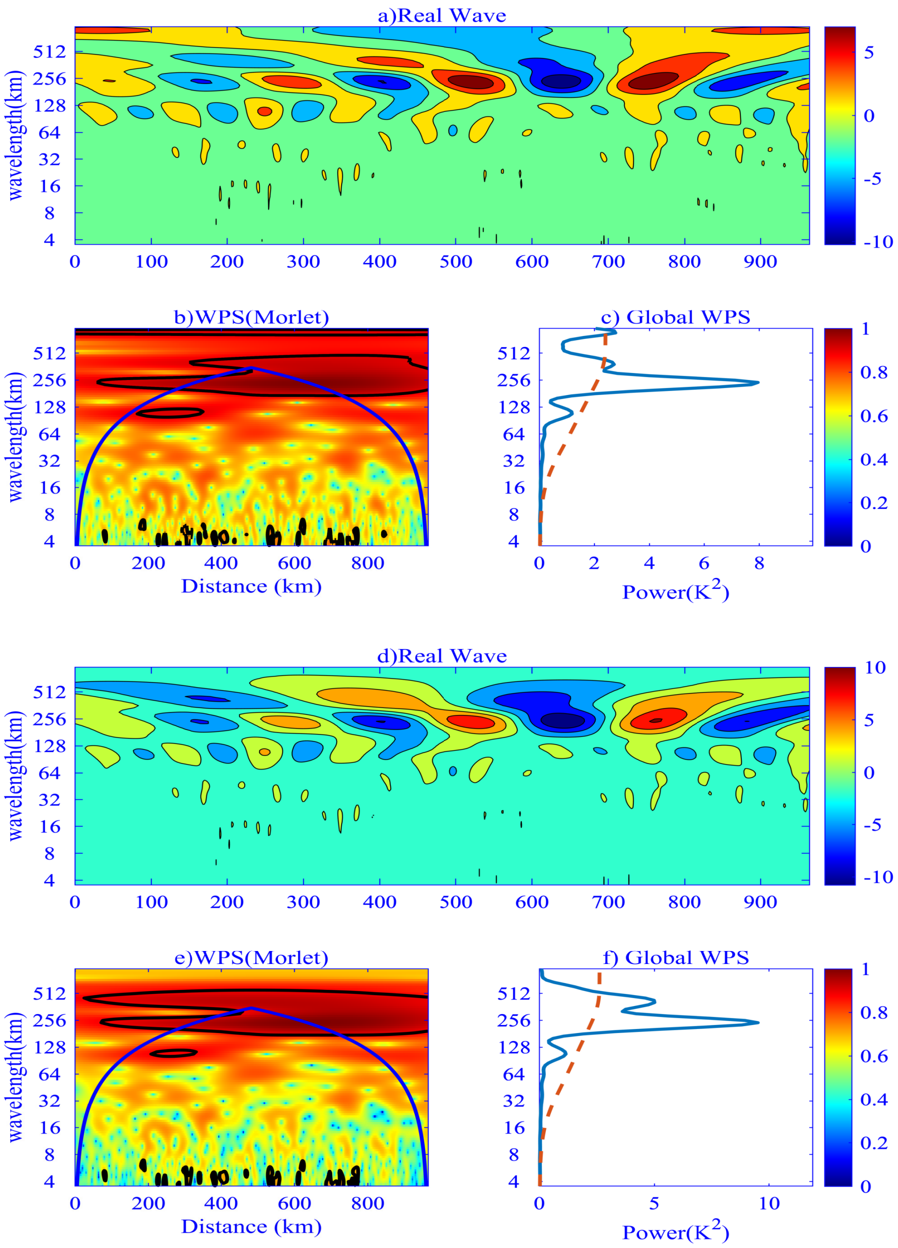

Figure 9. Wavelet coefficient and WPS (Local and Global) of the CI (a, b, c) and OPF(d, e, f) BT curves in Figure 7.

7 Appendix: OPF Method

The OPF method is based on Chebyshev polynomials and basis functions. The raw BT can be fitted as (Junkins et al., 2013; Li et al., 2019):

$$\tilde{T}(x_i, yi) = \sum_{K=0}^{K_0} \sum_{S=0}^{S_0} A_{K,S} \Phi_K(x_i) \xi_S(y_i) \tag{A.1}$$

where $x_i (i = 1, 2, \ldots, N)$ and $y_j (j = 1, 2, \ldots, M)$, and K and S are the orders of polynomials in the x and y directions, respectively. K_0 and S_0 are the corresponding cut-off

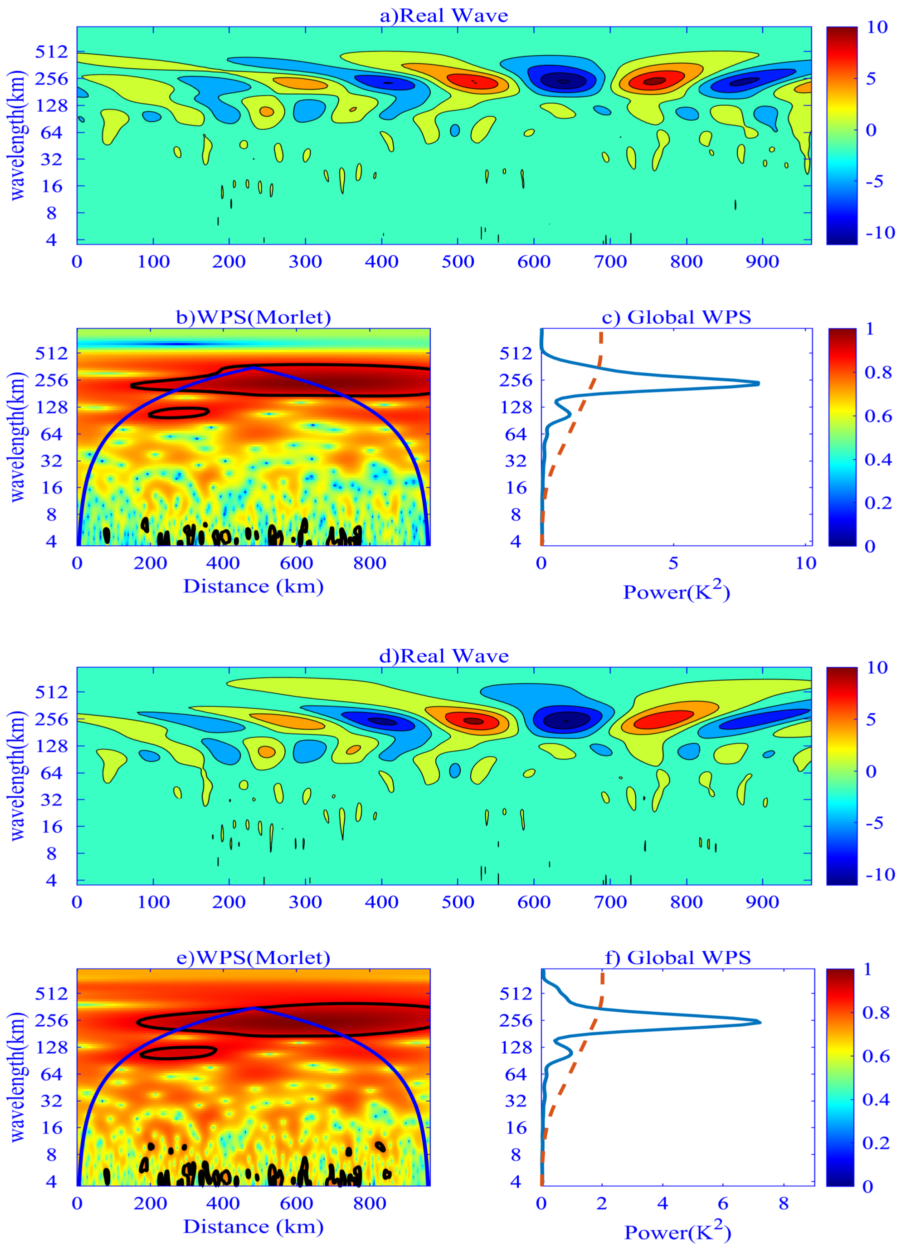

Figure 10. Wavelet coefficient and WPS (Local and Global) of the 5PF (a, b, c) and OPF (d, e, f) BT curves in Figure 7.

orders. $\Phi_K(x_i)$ is the k-order Chebyshev polynomial in the x direction, and $\xi_S(y_j)$ is the s-order Chebyshev polynomial in the y direction.

Because the Chebyshev polynomial is orthogonal, the Chebyshev expansion coefficients $A_{K,S}$ can be written as

$$A_{K,S} = \frac{\sum_{i=1}^{N}\sum_{j=1}^{M} T(x_i,y_i)\,\Phi_K(x_i)\,\xi_S(y_j)}{\sum_{i=1}^{N}\Phi_K(x_i)^2\sum_{j=1}^{M}\xi_S(y_j)^2} \tag{A.2}$$

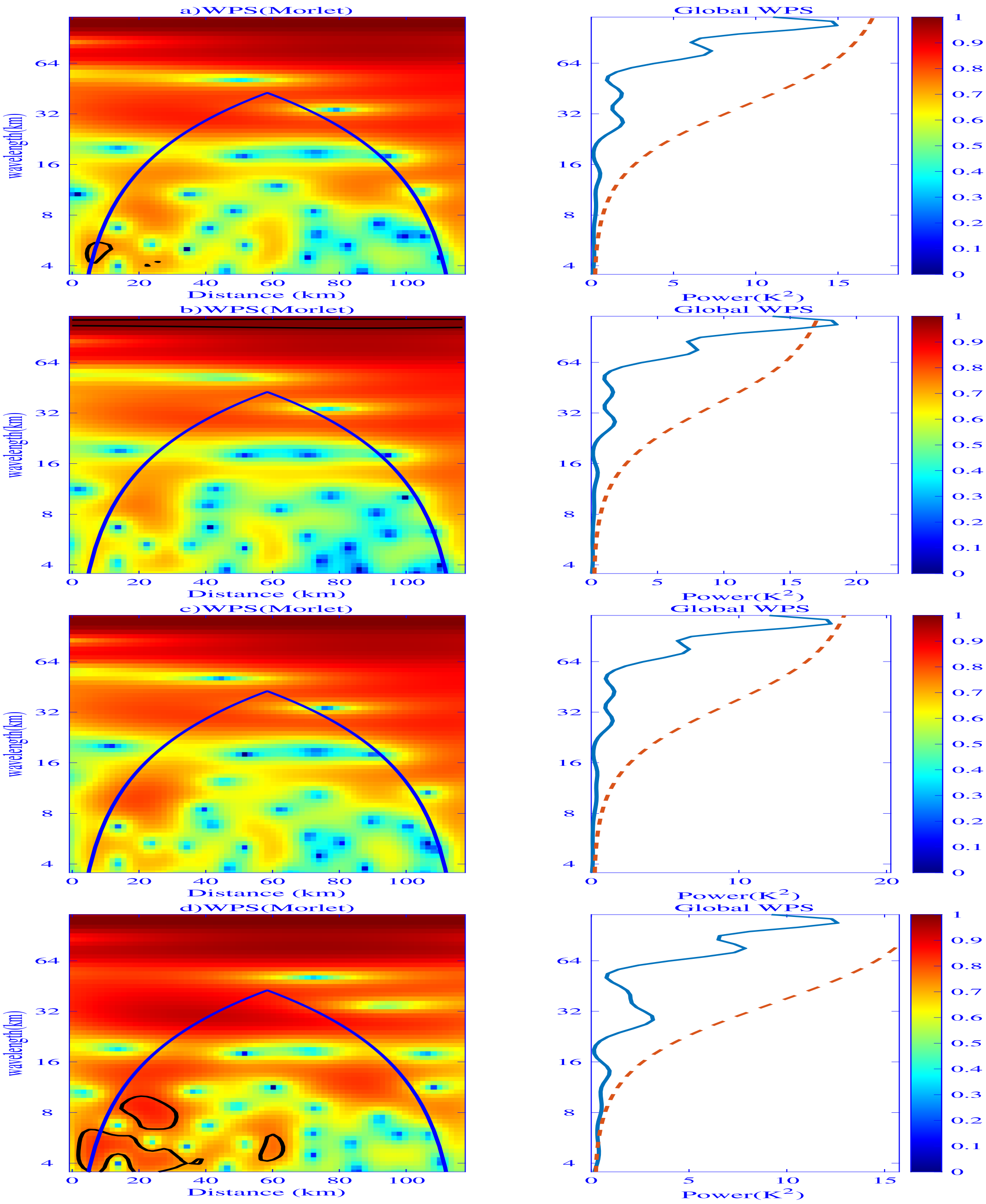

Figure 11. Local and Global WPS of the estimated BT by these four methods (a) CI, (b) 4PF, (c) 5PF and (d) OPF method at the right end of the curves in Figure 7.

The sum of squared errors SSE is expressed as

$$SSE(A_{0,0}, A_{1,0}, ..., A_{K_0,S_0}) = \sum_{i=1}^{N} \sum_{j=1}^{M} [T - \sum_{K=0}^{K_0} \sum_{S=0}^{S_0} A_{K,S}\, \Phi_K(x_i)\, \xi_S(y_j)]^2 \tag{A.3}$$

The raw BT is orthogonally expanded using the OPF method to determine the along-track and cross-track eigenvectors of each grid point, which are multiplied with the corresponding weight coefficients.

References

Alexander, M. J., and Barnet, C. Using satellite observations to constrain parameterizations of gravity waves effects for global models. *J. Atmos. Sci.***2007**, *64*, 1652–1665.

Alexander, M. J., Geller, M., McLandress, C., Polavarapu, S., Preusse, P., Sassi, F., Sato, K., Eckermann, S., Ern, M., Hertzog, A., Kawatani, Y., Pulido, M., Shaw, T. A., Sigmond, M., Vincent, R., and Watanabe, S. Recent developments in gravity-wave effects in climate models and the global distribution of gravity wave momentum flux from observations and models. *Q. J. Roy. Meteor. Soc.***2010**, *136*, 1103–1124.

Eckermann, S. D., and Preusse P. Global measurements of stratospheric mountain waves from space. *Science*1999, *286*, 1534–1537.

Eckermann, S. D., Wu, D. L., Doyle, J. D., Burris, J. F., McGee, T. J., Hostetler, C. A., Coy, L., Lawrence, B. N., Stephens, A., McCormack, J. P., and Hogan, T. F. Imaging gravity waves in lower stratospheric AMSU-A radiances, Part 2: Validation case study. *Atmos. Chem. Phys.***2006**, *6*, 3343–3362.

Fetzer, E. J., and Gille J. C. Gravity wave variance in LIMS temperatures. Part I: Variability and comparison with background winds. *J. Atmos. Sci.***1994**, *17*, 2461–2483.

Florian, Z., and Vincent, R. A. Wavelet analysis of stratospheric gravity wave packets over Macquarie Island: 1. Wave parameters. *J. Geophys. Res.***2001**, *106*, 289–297.

Hindley, N. P., N. D. Smith, C. J. Wright, D. Andrew, and Nicholas, J. M. A two-dimensional Stockwell transform for gravity wave analysis of AIRS measurements. *Atmos. Meas. Tech.***2016**, *9*, 2545–2565.

Hoffmann, L., and Alexander M. J. Retrieval of stratospheric temperatures from Atmospheric Infrared Sounder radiance measurements for gravity wave studies. *J. Geophys. Res.***2009**, *114*, D07105.

Hoffmann, L., and Alexander, M. J. Occurrence frequency of convective gravity waves during the North American thunderstorm season. *J. Geophys. Res.***2010**, *115*, D20111.

Hoffmann, L., Alexander, M. J., Clerbaux, C., Grimsdell, A. W., Meyer, C. I., Rößler, T., and Tournier, B. Intercomparison of stratospheric gravity wave observations with AIRS and IASI. *Atmospheric Measurement Techniques***2014**,*7(12)*, 4517–4537.

Hoffmann, L., X. Wu, and Alexander, M. J. Satellite observations of stratospheric gravity waves associated with the intensification of tropical cyclones. *J. Geophys. Res.***2018**, *45*, 1692–1700.

Holt, L. A., Alexander, M. J., Coy, L., Liu, C., Molod, A., Putmanb, W., and Pawsonb, S. An evaluation of gravity waves and gravity sources in the southern hemisphere in a 7 km global climate simulation. *Q. J. Roy. Meteor. Soc.***2017**, *143*, 2481–2495.

Hong, S. Y., J. Dudhia, and Chen, S. H. A revised approach to ice microphysical processes for the bulk parameterization of clouds and precipitation. *Mon. Weather Rev.***2004**, *132(1)*, 103–120.

Hong, S. Y., Y. Noh, and Dudhia, J. A new vertical diffusion package with an explicit treatment of entrainment processes. *Mon. Weather Rev.***2006**, *134(9)*, 2318–2341.

Junkins, J. L., A. B. Younes, and Bai, X. Orthogonal polynomial approximation in higher dimensions: Applications in astrodynamics. *Adv. Astronaut. Sci.***2013**, *147*, 531–594.

Li, B. T., Y. Z. Liu, X. Y. Wang, Q. J. Fu, and Lv, X. Q. Application of the Orthogonal Polynomial Fitting Method in Estimating PM2.5 Concentrations in Central and Southern Regions of China. *Int. J. Enviro. Res. and Public Health.***2019**, *16*, 1418.

Lyapustin, A., M. J. Alexander, L. Ott, A. Molod, B. Holben, J. Susskind, and Wang, Y. Observation of mountain lee waves with MODIS NIR column water vapor. *Geophys. Res. Lett.***2014**, *41*, 710–716.

Miller, S. D., W. C. Straka III, J. Yue, S. M. Smith, M. J. Alexander, L. Hoffmann, M. Setvák, and Partain, P. T. Upper atmospheric gravity wave details revealed in night-glow satellite imagery. *Proc. Nat. Acad. Sci.***2015**, *112*, E6728–E6735.

Moffat-Griffin, T. An introduction to atmospheric gravity wave science in the polar regions and first results from ANGWIN. *J. Geophys. Res.***2019**,*124*, 1198–1199.

Perrett, J. A., Wright, C. J., Hindley, N. P., Hoffmann, L., Mitchell, N. J., Preusse, P. Determining gravity wave sources and propagation in the Southern Hemisphere by ray-tracing AIRS measurements. *Geophys. Res. Lett.***2021**, *48*, 2020GL088621.

Uhlenbrock, N. L., K. M. Bedka, W. F. Feltz and Ackerman S. A. Mountain wave signatures in MODIS 6.7-μm imagery and their relation to pilot reports of turbulence. *Weather Forecasting***2007**, *22*, 662–670.

Vargas, F., J. L. Chau, H. Charuvil Asokan, and M. Gerding, M. Mesospheric gravity wave activity estimated via airglow imagery, multistatic meteor radar, and SABER data taken during the SIMONe–2018 campaign. *Atmos. Chem. Phys.***2021**, *21*, 13631–13654.

Wang, Y., L. F. Zhang, Peng, J. On the Spectra of Gravity Waves Generated by Two Typical Convective Systems. *Atmos.***2019**, *10*, 405.

Wright, C. J., Hindley, N. P., Hoffmann, L., Alexander, M. J., and Mitchell, N. J. Exploring gravity wave characteristics in 3-d using a novel s-transform technique: AIRS/aqua measurements over the southern andes and drake passage. *Atmos. Chem. Phys.***2017**, *17(13)*, 8553–8575.

Wu, D. L., and F. Zhang, F. A study of mesoscale gravity waves over the North Atlantic with satellite observations and a mesoscale model. *J. Geophys. Res.***2004**, *109*, D22104.

Wu, J. F., X. H. Xue, L. Hoffmann, X. K. Dou, H. M. Li, and T. D. Chen, T. D. A case study of typhoon-induced gravity waves and the orographic impacts related to Typhoon Mindulle (2004) over Taiwan. *J. Geophys . Res. Atmos.***2015**, *120*, 9193–9207.